AIAA JOURNAL
Vol. 30, No. 4, April 1992

Calculations of the Dilution System in an Annular Gas Turbine Combustor

J. J. McGuirk* and J. M. L. M. Palma†
Imperial College of Science, Technology and Medicine, London SW7 2BX, England, United Kingdom

The present work is concerned with the ability of a two-equation turbulence model (k-ϵ) of predicting accurately the mixing parameters at the outlet of an annular gas turbine combustor. A comparison between numerical and experimental results is presented with attention paid to numerical accuracy and boundary condition sensitivity. A numerical grid with 36,000 nodes was needed to resolve the flow inside a 7.5-deg annular sector. It was found that an insufficient number of grid nodes led to the underprediction of the streamwise vorticity and a different flow pattern in the wake and downstream of the jets. Two basic sets of calculations with constant and variable density are included. The calculations could predict the general features of the flow, but evidenced lower levels of mixing compared to the experiments, even with a reduction of the turbulent Prandtl number from 0.9 to 0.5.

Nomenclature

C_μ, C_1, C_2 = constants of k-ϵ turbulence model, $C_\mu = 0.09$, $C_1 = 1.44$, $C_2 = 1.92$
D = jet diameter
D/Dt = $\partial/\partial t + U_i \times \partial/\partial x_i$, = substantial derivative
F = source term
k = turbulence kinetic energy
L = length of the annulus
M_{ratio} = momentum flux ratio
$\dot{m}$ = mass flow rate
P = static pressure
R, r = cylindrical polar coordinates
S = spacing between holes
S/D = pitch to diameter ratio
T = temperature
T^* = nondimensionalized temperature, $(T - T_{\text{annulus}})/(T_{\text{jet}} - T_{\text{annulus}})$
T_{annulus} = mean inlet temperature of the annulus flow
T_{jet} = mean inlet temperature of the jets (mass weighted average temperature of the two jets)
T_{max} = maximum temperature at the outlet section
$T_{\text{max}}^{\text{radial}}$ = maximum circumferential temperature at the outlet section
T_{mean} = mean exit temperature
t = time
U = axial component of velocity
V = radial component of velocity
V_{ratio} = velocity ratio
W = aximuthal component of velocity
x_i = spatial coordinates in tensor notation
Z = cylindrical polar coordinate
Γ = diffusivity
Γ_{eff} = effective diffusivity, $\Gamma_t + \Gamma$
Γ_t = turbulent diffusivity, μ_t/σ_t
ΔD = size of the annular gap
δ_{ij} = Kronecker delta, 1 for $i = j$, 0 for $i \neq j$
ϵ = rate of dissipation of turbulence kinetic energy
η = mixedness parameter, $(1 - \sigma/\sigma_{\text{max}}) \times 100\%$
θ = cylindrical polar coordinate
μ = dynamic viscosity
μ_{eff} = effective viscosity, $\mu_t + \mu$
μ_t = turbulent viscosity, $\rho C_\mu k^2/\epsilon$
ν = kinematic viscosity
ρ = density
$\overline{\rho u_i c}$ = double correlation
$\overline{\rho u_i u_j}$ = Reynolds stresses
σ_k, σ_ϵ = constants of k-ϵ turbulence model, $\sigma_\epsilon = 1.0$, $\sigma_\phi = 1.3$
σ_t = turbulent Prandtl number, 0.9 and 0.5
Φ = passive scalar
Φ^* = nondimensionalized passive scalar, $(\Phi - \Phi_{\text{annulus}})/(\Phi_{\text{jet}} - \Phi_{\text{annulus}})$
Ψ = unmixedness parameter, $0.5\sigma/\sigma_{\text{max}}(T_{\text{annulus}} - T_{\text{jet}})/(T_{\text{mean}} - T_{\text{jet}})$
$\bar{}$ = time averaged quantity
$\partial/\partial x_i$, $\partial/\partial t$ = partial derivatives

Subscripts

i, j, k = indices of the tensorial notation
jet = jet velocity
ref = cross stream

Introduction

THE need to provide a suitable temperature distribution at the outlet has always been one of the major requirements in the design of gas turbine combustors.[1] This is usually achieved by the mixing of the hot combustion gases with jets of cold air injected through holes in the combustor walls.

The main flow parameter governing the mixing and penetration of the jets is the momentum flux ratio between jets and cross stream (e.g., see Ref. 2). The geometrical parameters of design are the number of holes, their diameter, and the spacing between the holes in jet diameters (pitch to diameter ratio). Geometrical variables, such as the angle of injection and the convergence of the walls, are also important, but are not included in the semiempirical correlations (e.g., see Refs. 2 and 3) often used in combustor design, which seriously limits their applicability and reinforces the interest in the use of computational fluid dynamics (CFD).

Received April 1, 1991; revision received May 21, 1991; accepted for publication July 8, 1991.

*Lecturer, Mechanical Engineering Department; currently, Professor of Aerodynamics, Loughborough University of Technology, Department of Transport Technology, Loughborough, Leicestershire LE11 3TU, England, United Kingdom.

†Research Student, Mechanical Engineering Department; currently, Assistant Professor, University of Oporto, Faculty of Enginering, Department of Mechanical Engineering and Industrial Management, Rua dos Bragas, 4099 Porto Codex, Portugal.

Khan et al.[4] discuss the results of an application of CFD to a dilution zone system. They find that some discrepancies between the experimental and numerical results give strong evidence of numerical errors caused by the coarseness of the grid; nevertheless, the effect of the tunnel height and jet spacing can be predicted by the model. Aspects affecting numerical accuracy, which require particular attention in the calculation of gas turbine dilution systems, are the distribution and level of grid refinement, the influence of the boundary condition used at the inlet plane of the jets, and the turbulence model.

The need for fine grids has been addressed, in the context of a single jet in crossflow, by many authors (e.g., see Refs. 5–7); Claus,[7] for instance, states that calculations with grids of $90 \times 40 \times 22$ (79,200 grid nodes) are still grid-dependent. This problem, however, is less critical in calculations of rows of jets because the flow pattern repeats transversely every half jet and only half of one jet is needed on the grounds of symmetry conditions.

The simplest boundary condition to use in the inlet plane of the dilution jets is to assume a constant velocity profile; this is known to be incorrect, especially for low-velocity ratios of 0.5 where the cross stream distorts the velocity profile at the inlet plane of the jet (e.g., see Ref. 8). White,[6] Demuren,[9] and Khan et al.,[4] in calculations with either a row of jets or a single jet configuration, tested various boundary conditions: plug flow profile, constant total pressure, and coupling between two sets of calculations (one inside the jet feed tube and the other with the actual jet in crossflow). White[6] strongly favors coupling between the two sets of calculations, but the complexity of this approach has led investigators to prefer the constant total pressure boundary condition, or simply a plug flow velocity. This problem is more critical in real combustor geometries since the dilution holes are fed through an annulus and deviations from the plug flow assumption are likely to occur. Calculations of real combustors might have to be done in a domain of integration incorporating both the interior of the combustor and the annular passages feeding the holes in the combustor walls, as made in Green and Whitelaw[10] and Manners.[11]

Many authors have commented on limitations of the turbulence model in this type of flow, but the importance of the problems just mentioned has hindered progress in this area. Two aspects of the turbulence model need to be distinguished here: the modeling of the turbulent transport of momentum and the modeling of the turbulent transport of scalars, the scalar flux model. The latter directly affects the prediction of the mixing parameters, particularly in regions without chemical reaction, since the equation of conservation of a passive scalar is simply a balance between convection and diffusion, i.e., turbulent transport. In case of gradient type models (the k-ϵ model is generally used), the ratio between the diffusion coefficients of momentum and scalars is given by the turbulent Prandtl number and, although 0.9 is normally used, there are some doubts about the appropriate value of the turbulent Prandtl number in recirculating flows.[12] At the present, the simple expedient of reducing its value for a better agreement with the experimental results has often been used (e.g., see Ref. 13).

The present study is concerned with the ability of the k-ϵ turbulence model to accurately predict the mixing parameters at the outlet of an annular gas turbine combustor. Previous works by Mongia et al.[14] and McGuirk[15] called our attention to some particularities in the calculation of dilution zones requiring clarification. Mongia et al.[14] found that there was no need for fine grids; in the results of preliminary calculations, McGuirk[15] failed to show the hot spots at the outlet section aligned with the jet axis. The need to find an explanation for these results provided the initial motivation for the present work; however, other aspects soon emerged of interest to the calculation of dilution zones that will also be addressed in this study.

Mathematical Model

Governing Equations

The equations governing the fluid motion of an incompressible, constant property, Newtonian fluid, and the transport of a scalar are, in an Eulerian description and after Reynolds average (cf. Hinze[16]),

$$\frac{\partial U_i}{\partial x_i} = 0 \tag{1}$$

$$\rho \frac{DU_i}{Dt} = -\frac{\partial P}{\partial x_i} + \frac{\partial}{\partial x_j}\left[\mu\left(\frac{\partial U_i}{\partial x_j} + \frac{\partial U_j}{\partial x_i}\right) - \rho\overline{u_i u_j}\right] + F_i \tag{2}$$

$$\rho \frac{D\Phi}{Dt} = \frac{\partial}{\partial x_i}\left(\Gamma \frac{\partial \Phi}{\partial x_i} - \rho\overline{u_i \phi}\right) + F_\phi \tag{3}$$

The Reynolds stresses $\rho\overline{u_i u_j}$ are related to the local strain rate through the Boussinesq eddy viscosity concept:

$$\rho\overline{u_i u_j} = \frac{2}{3}\rho k \delta_{ij} - \mu_t\left(\frac{\partial U_i}{\partial x_j} + \frac{\partial U_j}{\partial x_i}\right) \tag{4}$$

The double correlation $\rho\overline{u_i \phi}$ is approximated by

$$-\rho\overline{u_i \phi} = \Gamma_t \frac{\partial \Phi}{\partial x_i} \tag{5}$$

The modeled equations for the transport of momentum and scalar quantities then revert to

$$\rho \frac{DU_i}{Dt} = -\frac{\partial P}{\partial x_i} + \frac{\partial}{\partial x_j}\left[\mu_{\text{eff}}\left(\frac{\partial U_i}{\partial x_j} + \frac{\partial U_j}{\partial x_i}\right)\right] + F_i \tag{6}$$

$$\rho \frac{D\Phi}{Dt} = \frac{\partial}{\partial x_i}\left(\Gamma_{\text{eff}} \frac{\partial \Phi}{\partial x_i}\right) + F_\phi \tag{7}$$

The transport equation for temperature is identical to the equation used for the transport of a passive scalar Φ. In the latter, solution of the scalar equation could not feed back into the velocity equations via the density, whereas in case of variable density calculations, this was allowed to happen.

The turbulence kinetic energy k and its rate of dissipation ϵ are determined from the following modeled equations[17]:

$$\rho \frac{Dk}{Dt} = \frac{\partial}{\partial x_i}\left(\frac{\mu_t}{\sigma_k} \frac{\partial k}{\partial x_i}\right) - \rho\overline{u_i u_j} \frac{\partial U_i}{\partial x_j} - \rho\epsilon \tag{8}$$

$$\rho \frac{D\epsilon}{Dt} = \frac{\partial}{\partial x_i}\left(\frac{\mu_t}{\sigma_\epsilon} \frac{\partial \epsilon}{\partial x_i}\right) - \frac{\epsilon}{k} C_1 \rho\overline{u_i u_j} \frac{\partial U_i}{\partial x_j} - C_2 \rho \frac{\epsilon^2}{k} \tag{9}$$

For numerical solution of Eqs. (8) and (9), a methodology similar to that described in detail by Patankar[18] was followed. The discretization of these transport equations was accomplished using finite difference techniques in a staggered grid system. The diffusion and the convective terms were approximated by a central and hybrid differencing scheme, respectively.

Domain of Integration: Numerical Grids

The experimental geometry[19] (Fig. 1) consisted of an annular duct (with a total of 48 equally spaced directly opposed holes, equally divided between outer and inner wall) followed by a convergent nozzle. For numerical simulation, a cylindrical polar system of coordinates was used with the longitudinal axis aligned with the engine axis. The domain of integration was extended over a circumferential sector of either 15 or 7.5 deg, depending on the boundary conditions. The holes and the sloped walls of the nozzle were approximated by cells of rectangular shape. The fluid density for the cells inside the hole was multiplied by the ratio between the area of the hole and the total area of the cells inside the hole to guarantee similar numerical and experimental flow rates.

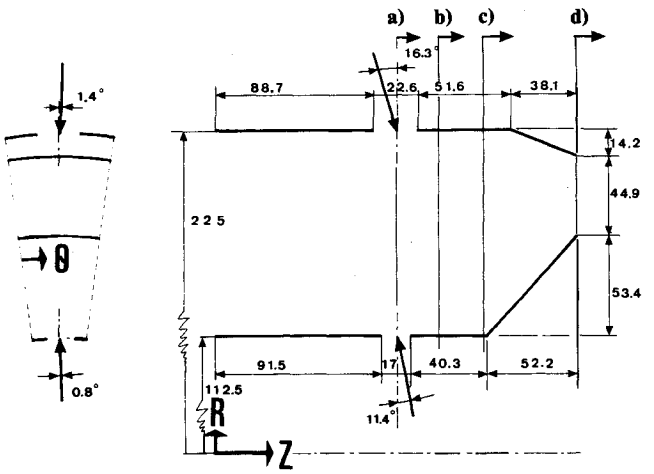

Fig. 1 Geometry of the annular dilution system (dimensions in mm): flow splits, inclination of the jets, and exact location of the cross-sectional views (a: $z = 100$ mm; b: $z = 123.6$ mm; c: $z = 147.6$ mm; d: $z = 201$ mm).

Four numerical grids (Table 1), nonuniform along all of the directions, were used. The coarsest grid, $17 \times 11 \times 6$, was used to set up the boundary conditions and to illustrate the effects of insufficient numerical resolution. The two grids, $40 \times 30 \times 15$ and $40 \times 30 \times 30$, were the standard ones for calculations over a 7.5- and a 15-deg sector, respectively. The finest grid, $70 \times 40 \times 25$, occupied all of the memory available on the computer hardware and was used only as a check on the numerical accuracy of the standard mesh predictions.

Boundary Conditions

Table 2 shows the boundary conditions used in the present calculations and set according with the experiments of Shaw[19] (see Palma[20] for details). In case 1, the radial and tangential components of velocity at the jet entries were both set to zero and a circumferential sector of 7.5 deg was used with symmetry conditions on the two extreme constant θ planes. These conditions were probably too simplistic; in particular, the measurements of Shaw[19] showed an inclination of the jets with respect to the hole geometric axis. Averaging of the measurements of these jet angles leads to the values also shown in Fig. 1, which enabled the use of boundary conditions in the holes, with both axial and tangential velocities specified as well as the radial inflow component. Under these conditions (cases 2 and 3), a 15-deg sector was needed, limited by the two longitudinal planes halfway between the jets; cyclic boundary conditions were now implemented on these planes. For these conditions, calculations were carried out assuming variable density (case 3). The turbulence kinetic energy and its dissipation were set to give an eddy viscosity at inflows corresponding to a level of order 100 times the molecular viscosity to represent fully turbulent inflow streams. Experience in jet-in-crossflow and internal combustor flowfield predictions usually shows that the turbulence boundary conditions are of only minor significance due to the high levels of turbulence generated internally as a result of curved shear layers, jet impingement, etc.

The simplicity of the boundary conditions in the holes, with constant values specified in the hole surface for all of the variables, contrasts with more elaborate treatments used in some calculations of jets in crossflow geometries (see the Introduction); however, in the present application, this was considered as satisfactory since the values were based as far as possible on experimental data.

The cells adjacent to the plane walls were treated by the wall functions.[21] In cells along the staircase approximation, the convective and diffusive fluxes were set to zero without using wall functions.

At the outlet section, a zero axial gradient was used as the boundary condition for all of the variables and this led, relative to the experimental rig, to a plane extension duct at the nozzle exit to avoid the propagation of this artificial boundary condition into the internal flow.

Discussion of Results

Because of the complexity of the flow, the numerical results are shown mainly as surface views and integral parameters of mixing as defined in the Nomenclature. The velocity and scalar fields are illustrated by streakline and contour plots, respectively. The discussion of the results forms two main subsections with constant and variable density calculations. In the first subsection, the numerical accuracy is assessed by comparing the results obtained with various grids of different resolution, followed by the results of cases 1 and 2. The results in the second subsection (case 3) consider the variations of density as a local function of temperature. Finally, different turbulent Prandtl numbers are tried in an attempt to examine the sensitivity of the predicted results to the part of the turbulence model that directly affects scalar mixing.

Table 1 Numerical grids

Number	Grid size, $N_Z \times N_R \times N_T$[a]	Number of nodes	Number of cells inside the holes	L/N_Z,[b] mm	R/N_R,[b] mm	T/N_T,[b] deg
1	$17 \times 11 \times 6$	1,122	19	14.7	10.2	1.3
2	$40 \times 30 \times 15$	18,000	121	6.3	3.7	0.5
3	$40 \times 30 \times 30$	36,000	228	6.3	3.7	0.5
4	$70 \times 40 \times 25$	70,000	282	4.0	2.8	0.3

[a] N_Z, N_R, N_T: number of nodes along the axial, radial, and circumferential directions, respectively.
[b] L, R, T: dimensions of the integration domain along the three directions above.

Table 2 Boundary conditions of the annular dilution system and momentum flux and velocity ratio between the jets and the annular flow[a]

Case	Annulus U	Annulus V	Annulus W	Inner jet U	Inner jet V	Inner jet W	Outer jet U	Outer jet V	Outer jet W	$\dot{M}_{ratio}$[b]	V_{ratio}[c]
1	10.9	0	0	0	67.2	0	0	−75.5	0	42.7	6.5
	$\rho = 1.18$			$\rho = 1.18$			$\rho = 1.18$				
2	10.9	0	0	−13.3	67.2	−0.9	20.9	−73.5	−1.8	42.7	6.5
	$\rho = 1.18$			$\rho = 1.18$			$\rho = 1.18$				
3	32.4	0	0	−18.0	90.8	−1.3	24.3	−90.2	−2.2	18.6	2.8
	$\rho = 0.39$			$\rho = 0.87$			$\rho = 0.96$				

[a] All runs with $T_{annulus} = 900$ K, $T_{inner} = 363$ K, and $T_{outer} = 400$ K.
[b] Momentum flux ratio between the jets and the crossflow.
[c] Velocity ratio between the jets and the crossflow.

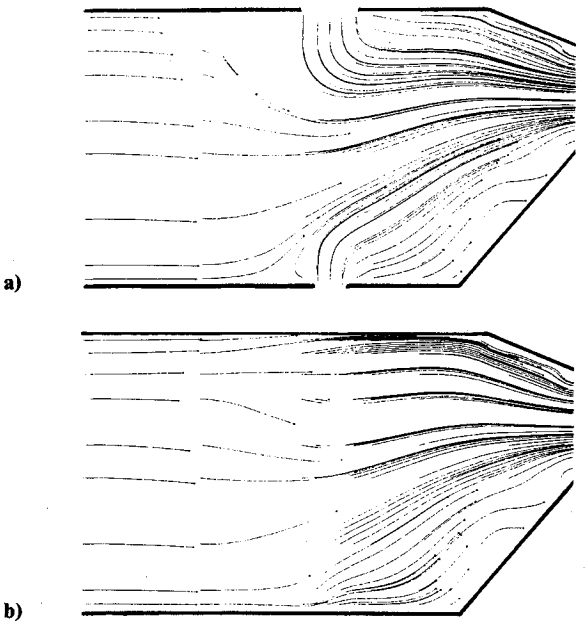

Fig. 2 Streakline plots—longitudinal views ($17 \times 11 \times 6$ grid) (case 1): a) center plane; b) midplane.

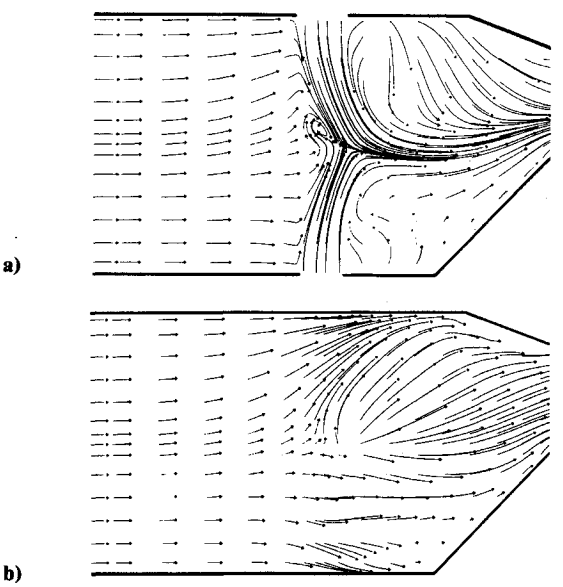

Fig. 3 Streakline plots—longitudinal views ($40 \times 30 \times 15$ grid) (case 1): a) center plane; b) midplane.

Constant Density Calculations

Figures 2–4 show the streaklines along the streamwise direction in the two extreme θ planes: $\theta = 7.5$ deg, the plane containing the axis of the holes (referred to as the center longitudinal plane); and $\theta = 0$ deg, halfway between the holes (referred to as the mid longitudinal plane). These figures include results from calculations using three numerical grids. The coarsest grid in Figs. 2 shows, compared with Figs. 3, higher numerical diffusion (smoother trajectory of the particles) and, because of the reduced number of nodes, is unable to capture the small recirculation zone at midheight upstream of the impingement region of the jets (see Figs. 3 and 4). The coarsest grid is clearly unsuitable to calculate this flow.

The pattern in Figs. 4 corresponds to the finest grid with 62 and 4 times more nodes than the grids used in the calculations of Figs. 2 and 3, respectively. The longitudinal flow pattern (Figs. 3 and 4) and the passive scalar fields (Figs. 5 and 6) predicted by the two finer grids (grids 2 and 4) are very similar.

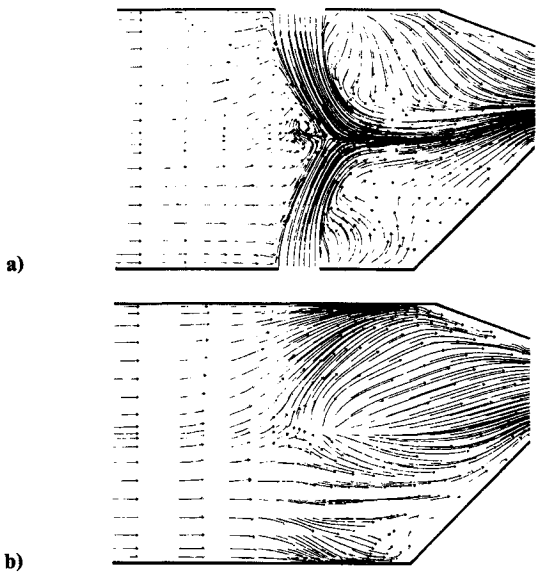

Fig. 4 Streakline plots—longitudinal views ($70 \times 40 \times 25$ grid) (case 1): a) center plane; b) midplane.

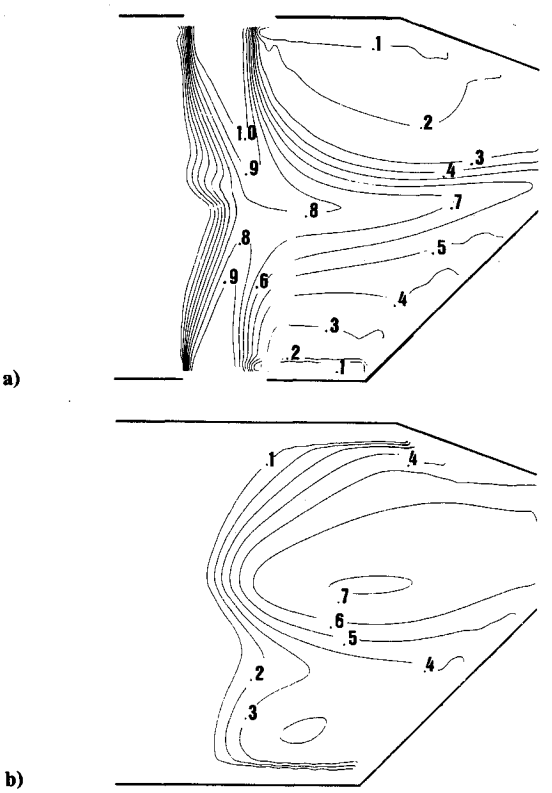

Fig. 5 Longitudinal contours of Φ^* ($40 \times 30 \times 15$ grid) (case 1): a) center plane; b) midplane.

Central differencing was used, in the case of the finest grid, over a large part of the integration domain (Figs. 7): the higher Peclet numbers (above 10) are concentrated at the edges and upstream of the jets for the radial and axial directions, respectively; similarity between the scalar fields of the two finer grids shows that the Peclet number distribution is similar in both grids.

The calculations in the finest mesh required about 40 h of CPU time (i.e., over a period of 1 month) to converge (AMDHAL 470/V8) and this, considering also the small differences between the results of the two meshes, led to the acceptance of the $40 \times 30 \times 15$ grid as accurate enough. The calculations were considered as converged only when the integrated flux of

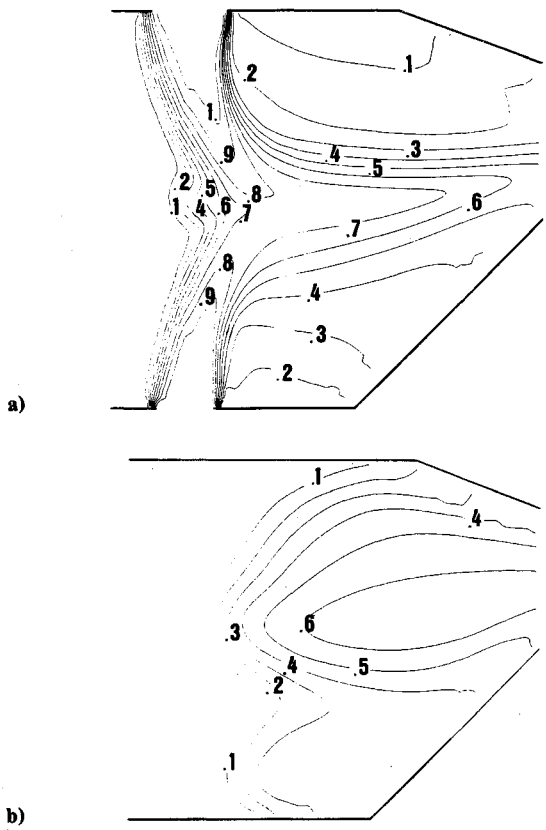

Fig. 6 Longitudinal contours of Φ^* ($70 \times 40 \times 25$ grid) (case 1): a) center plane; b) midplane.

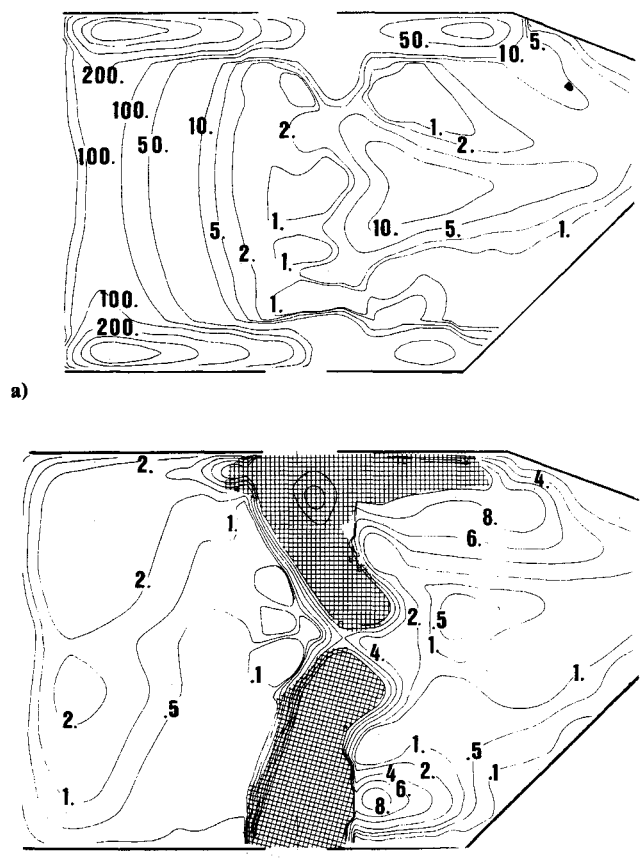

Fig. 7 Peclet number contours on center plane ($70 \times 40 \times 25$ grid) (case 1): a) axial direction; b) radial direction.

the scalar (passive scalar or temperature) was the same (within 2%) in every transverse cross section. This is a more stringent criterion of convergence than that based on the sum of the nondimensional mass residual over all the integration domain. It is obvious that the convergence of scalar variables, especially if they have a little influence on the momentum and continuity equations, can only be achieved after the velocity fields have been established, and the previous criterion was satisfied only after the nondimensional mass residual had been reduced to values of an order of 10^{-5}; this is two orders of magnitude lower than the criterion of convergence used by Mongia et al.[14] and probably explains some of the discrepancies between this and the present work.

The calculations with inclined jets (case 2) were initially made on a grid of $40 \times 30 \times 15$, which reduced the numerical resolution along the angular direction, because the integration domain extended over a 15-deg instead of a 7.5-deg sector. The streaklines of this calculation (in Figs. 8) have two salient features relative to the case with noninclined jets (Figs. 3): a steeper penetration of the bottom jet and, in its wake, a recirculation zone that extends over the whole sector (Fig. 8b). The different trajectory of the jets is a consequence of their misalignment in the longitudinal plane (Fig. 1): the bottom and top jets have upstream and downstream components, respectively. However, there seems to be no reason for the vortex in the wake of the bottom jet. To see whether this could be caused by the increased spacing between the nodes in the angular direction, calculations were made with noninclined jets, symmetry boundary conditions, in a sector of 15 deg, twice of what was actually needed—a condition designated by double symmetry.

In the absence of effects caused by the grid distribution, both symmetry and double symmetry conditions should give strictly identical results. However, Figs. 3 and 9 clearly indicate that they do not. The vortex in the wake of the bottom jet reappears in the case of double symmetry conditions, leading to a more uniform distribution of the passive scalar, as can be seen by comparing Figs. 5 and 10. The transverse cross-sectional views for both conditions (Figs. 11 and 12) provide an explanation for this phenomenon. The most evident feature of these figures is the region of streamwise vorticity in the upper half of the annulus created by the spanwise deflection of the jets, which still persists at the outlet section. A similar structure in the lower half is very much reduced because of both the smaller gap (pitch to diameter ratio) between jets on the inner wall and the blockage effect caused by the nozzle, creating an

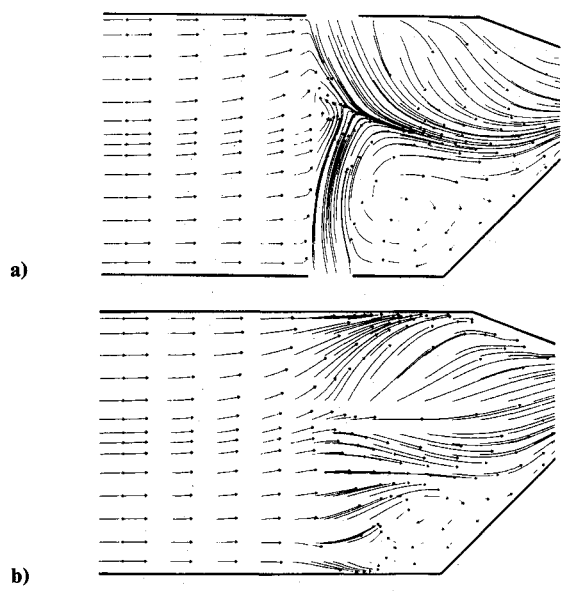

Fig. 8 Streakline plots—longitudinal views ($40 \times 30 \times 15$ grid), inclined jets: a) center plane; b) midplane.

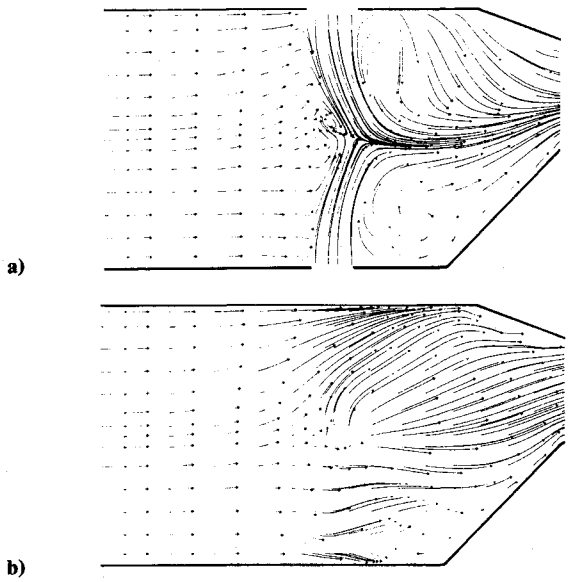

Fig. 9 Streakline plots—longitudinal views (40 × 30 × 15 grid), double symmetry: a) center plane; b) midplane.

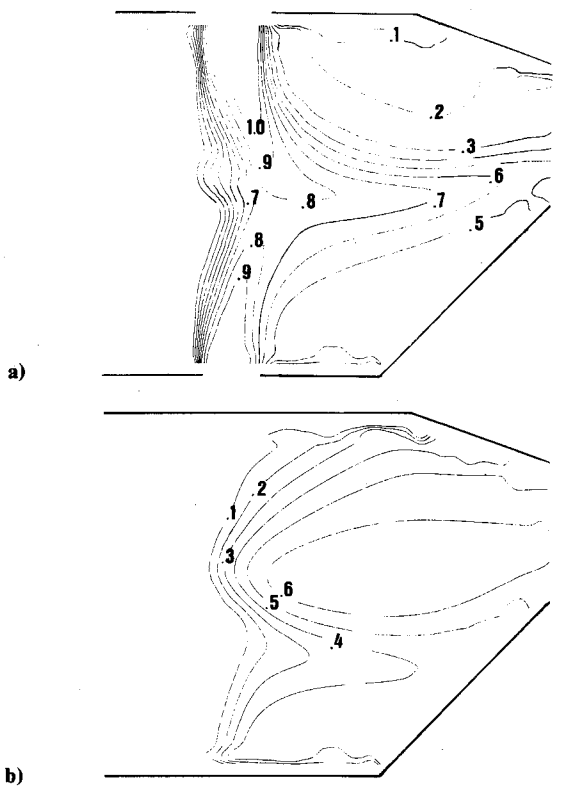

Fig. 10 Longitudinal contours of Φ^* (40 × 30 × 15 grid), double symmetry: a) center plane; b) midplane.

upward motion of the flow over most of the lower half of the annulus. The particles were released at every angular location and it is clear that, in the case of double symmetry conditions (Figs. 12), there are not enough grid lines to resolve the small vortex formed between the midplane and the edges of the bottom jet (compare Figs. 11a and 12a, the views containing the axis of the holes). Farther downstream (Fig. 11b), there is a tangential flow along the inner wall directed toward the center plane, whose magnitude is reduced in the case of the double symmetry conditions (Fig. 12b), where the particles mainly follow a radially outward trajectory. The magnitude of the azimuthal component of velocity is generally lower over most of this plane, and this is considered evidence of artificial

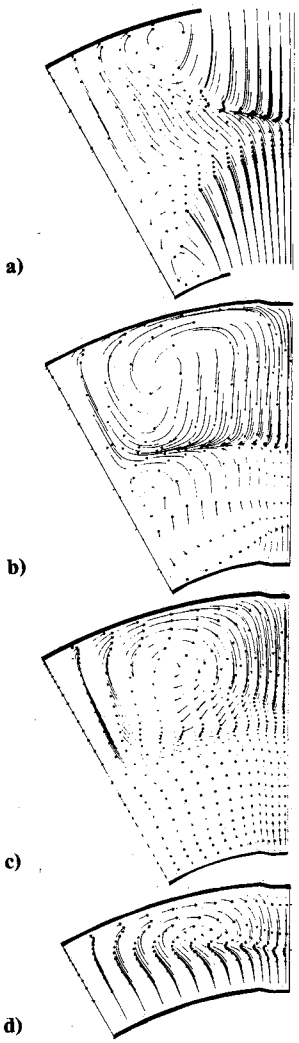

Fig. 11 Streakline plots—cross-sectional views (40 × 30 × 15 grid), symmetry (case 1): a) z = 100 mm; b) z = 123.6 mm; c) z = 147.6 mm; d) z = 201 mm. (Note that the cross-sectional views were magnified by 4 along the angular direction for the purpose of plotting, and therefore the 7.5- and 15-deg sectors appear as 30- and 60-deg sectors.)

diffusion, responsible for a higher decay rate of the secondary flows. Closer to the nozzle, the symmetry conditions (Fig. 11c) show a radially outward flow, which is reversed in the case of the double symmetry (Fig. 12c), since this location corresponds to the downstream end of the jet wake.

As proof of the correctness of the program, note in Figs. 12 that all of the particles released either on the center or on the midlongitudinal plane follow an exact radial trajectory, with no lateral deflection, and the two halves of the figures are mirror images of each other. The boundary conditions at the longitudinal planes of symmetry consist of setting to zero the normal gradients of the scalar quantities and velocity components parallel to the plane. The component of velocity normal to the plane, the azimuthal component in the present case, is also set to zero. This boundary condition is responsible in the upper half (Figs. 12a and 12b) for a sharper trajectory of the particles compared to Figs. 11, as opposed to what would be expected from a solution with higher numerical diffusion. Near the inner wall, because the number of grid lines between the midplane and the edges of the jet is small (only 2), a radial flow is enforced due to the boundary condition $W = 0$, the vortex is simply destroyed, and some of the cross-stream fluid that, by flowing around the base of the jet should fill the low pressure region in the wake of the bottom jet, is diverted to outer radial locations, therefore forcing the jet fluid to be recirculated and enlarging the jet wake. This can be confirmed

in the longitudinal contour plots through the relatively high and uniform scalar value of 0.5 in the wake of the jet (Figs. 10 compared to the symmetry conditions, Figs. 5). There are some difficulties in setting up a laboratory experiment with symmetry conditions, and the wake enlargement and apparent coalescence of the jets have also been observed experimentally in a row of jets.[22] Stringent tolerances are needed to ensure that a symmetric flow pattern exists downstream of the plane of the jets, and if two jets in the row are closer to each other, they tend to merge, increasing the blockage of the crossflow and giving rise to a wake region larger than what is found in a single jet.

The flow pattern in the longitudinal planes (Figs. 13), resulting from calculations with inclined jets using the new grid of $40 \times 30 \times 30$, confirms the steeper penetration of the inner jet and the vortex motion in the wake of the inner jet; this extends over the 15 deg of the sector, but is of a smaller size than that predicted by similar calculations on a coarser grid, $40 \times 30 \times 15$ (Figs. 8). The sensitivity demonstrated by the results to a slight inclination of the jets is proof of the accuracy of the calculations and an example of the role that CFD can play in the design of combustors. However, on the other hand, this sensitivity poses an extra strain on the appraisal of turbulence models on this type of geometry requiring very detailed and accurate measurements of the inlet conditions (since small alterations of the boundary conditions may produce alterations of the flow higher than the ones caused by the modifications of the turbulence model).

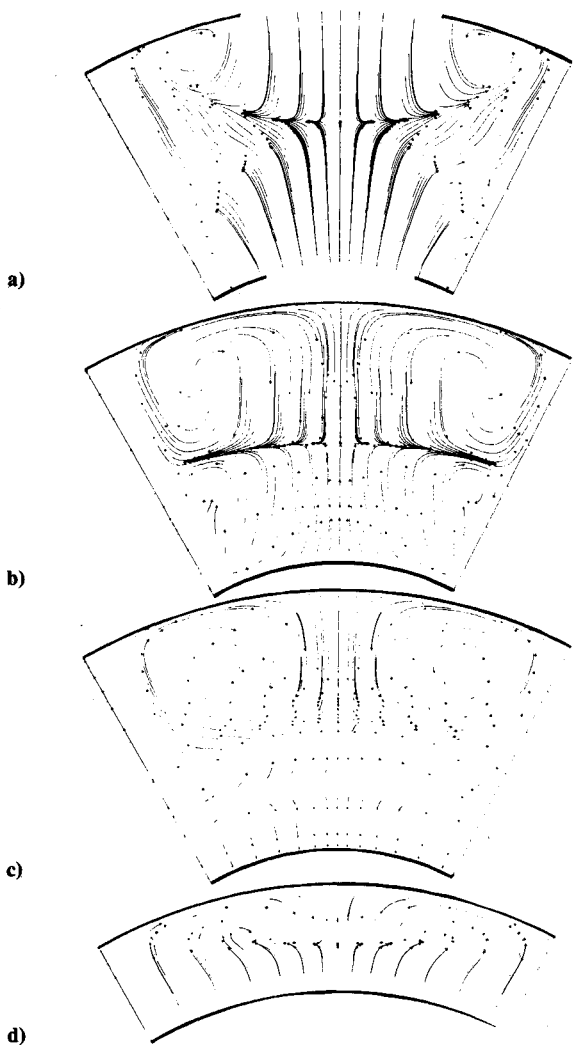

Fig. 12 Streakline plots—cross-sectional views ($40 \times 30 \times 15$ grid), double symmetry: a) $z = 100$ mm; b) $z = 123.6$ mm; c) $z = 147.6$ mm; d) $z = 201$ mm.

The main conclusion of this section is the proof that satisfactory accuracy can be achieved with grids of $40 \times 30 \times 15$ and $40 \times 30 \times 30$ to resolve the 7.5- and 15-deg sectors, respectively. The insufficient number of nodes can show either through the inability of the grid to resolve small scale features

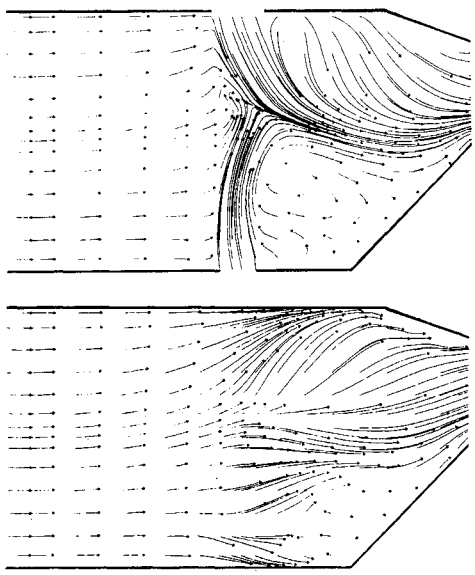

Fig. 13 Streakline plots—longitudinal views ($40 \times 30 \times 30$ grid), inclined jets (case 2): a) center plane; b) midplane.

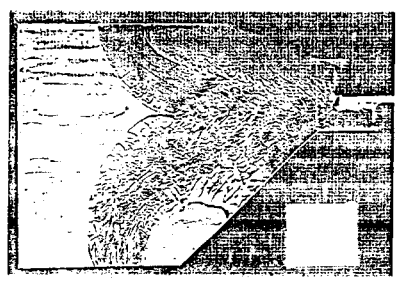

Fig. 14a Flow visualization (from experiments by Shaw[19]).

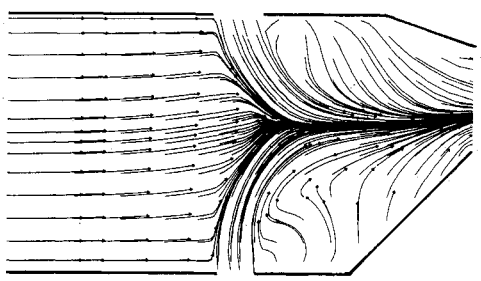

Fig. 14b Streakline plots—longitudinal views ($40 \times 30 \times 30$ grid), variable density calculations, inclined jets (case 3), center plane.

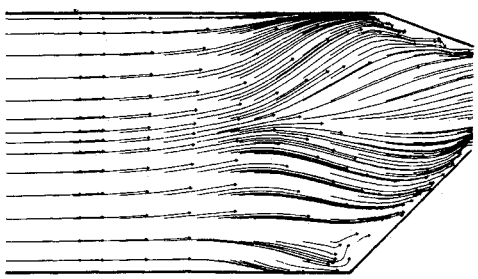

Fig. 14c Streakline plots—longitudinal views ($40 \times 30 \times 30$ grid), variable density calculations, inclined jets (case 3), midplane.

of the flow or through the lower magnitude of the azimuthal component of velocity that, associated with the boundary conditions in the longitudinal planes of symmetry, may promote the coalescence of the jets and lead to the appearance of spanwise vorticity in their wake. The conclusions of the work by Mongia et al.[14] that a grid with only four cells to simulate the hole was enough to calculate the flow inside a dilution zone system is not supported by the present work. In Mongia et al.,[14] the better agreement between experiment and predictions in case of coarse grids may have been the consequence of fortuitous circumstances that preclude the acceptance of their conclusions as generally valid.

Variable Density Calculations

The final calculation (case 3) is the one that most closely simulates the experiments: the variation of the density with the temperature and the inclination of the jets have both been taken into account. The density was evaluated at every point from the equation of state of an ideal gas. The fluctuations on mean density were still ignored. The normal velocities at every entry of the combustor (Table 2) were calculated using the air density corresponding to the temperature of the respective stream in order to maintain the same mass flow rate as the experiments. This also guarantees the same mass flow rate as in cases 1 and 2 but leads to a momentum flux ratio between the jets and the crossflow of 18.6 compared to 42.7 in case of constant density calculations.

The longitudinal flow pattern is shown in Figs. 14 and, relative to the previous calculation with constant density (Figs. 13), the most important features are the absence of the small recirculation zone upstream of the jets and the increased downstream bending of the jets. The experimental flow visualization, in Fig. 14a, although of poor quality, enables us to confirm these two features.

The cross-sectional views are shown in Figs. 15. Broadly speaking, the flow pattern is similar to the one shown in Figs. 12. The inclination of the jets is noticed (Fig. 15a) by the impingement closer to the outer wall, and the location of the center of the top vortices shifted toward the left and at a higher radial location. In Fig. 15b, the tangential flow along the inner wall is evident. The tangential motion along the inner wall, formed mainly by cross-stream fluid, penetrates between the jets in the regions near the walls (note the areas limited by the 0.1 and 0.2 contours in Figs. 16b and 16c), flows around the jets, and fills the wake region, being entrained by the jet fluid and following a radial trajectory along the axis of the jets. This explains why at the outlet section (Fig. 16d) the low value contours, corresponding to the cross-stream fluid, occur in the longitudinal center plane, i.e., aligned with the holes. The higher concentration fluid either spreads along the inner wall or bifurcates, depending on whether it is originated from the bottom or the top jet, respectively. When bifurcating, it then gives rise to the formation of the two regions of lower

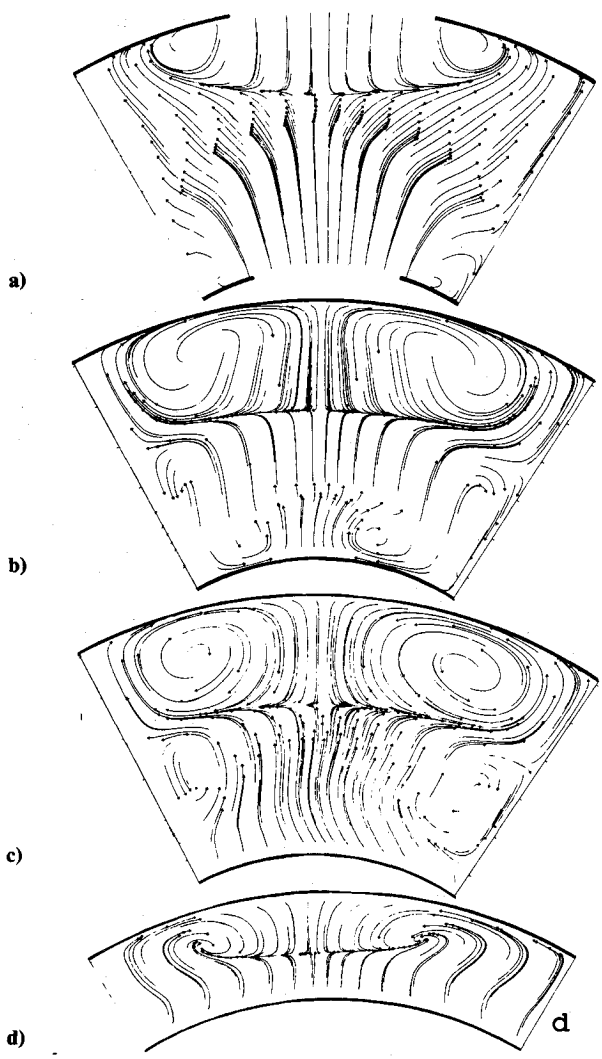

Fig. 15 Streakline plots—cross-sectional views (40 × 30 × 30 grid), variable density calculations, inclined jets (case 3): a) z = 100 mm; b) z = 123.6 mm; c) z = 147.6 mm; d) z = 201 mm.

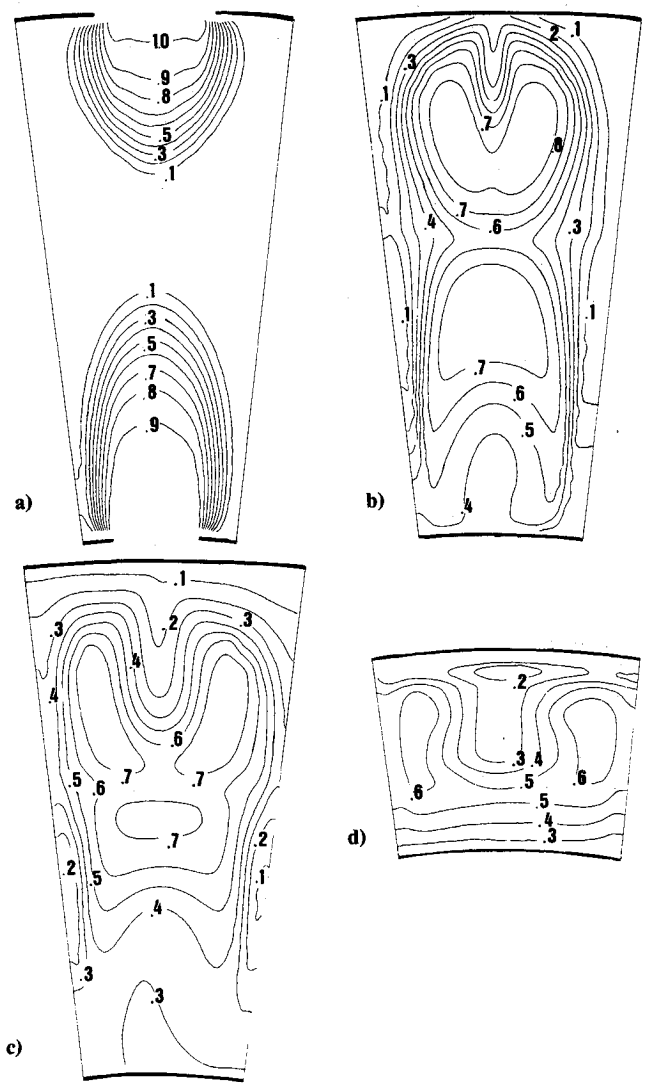

Fig. 16 Contours of T^*, cross-sectional views (40 × 30 × 30 grid), variable density calculations, inclined jets (case 3): a) z = 100 mm; b) z = 123.6 mm; c) z = 147.6 mm; d) z = 201 mm.

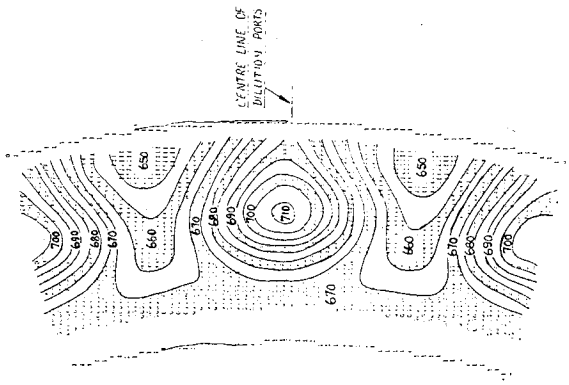

a) Experimental values from Shaw[19]

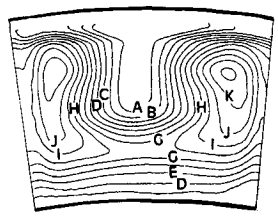

b) Predicted values (case 3), turbulent Prandtl number equal to 0.9 (A = 760 K; B = 740 K; C = 720 K; D = 700 K; E = 680 K; F = 660 K; G = 640 K; H = 620 K; I = 760 K; J = 600 K; K = 580 K)

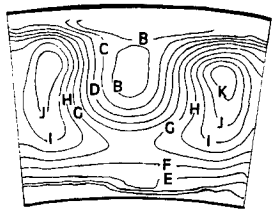

c) Predicted values (case 3), turbulent Prandtl number equal to 0.5

Fig. 17 Temperature contours at the outlet section.

temperature (higher T^*) in the region between the axes (the midlongitudinal plane). It is believed that the failure to resolve this sequence, which may be caused by insufficient grid nodes between the jet edges and the midlongitudinal plane, was the reason why the preliminary calculations of McGuirk[15] did not show the fluid originating from the cross stream aligned with the jet axis at the outlet section.

For a comparison with the experimental values (Fig. 17a), the temperature at the outlet section is also plotted in a dimensional form (Figs. 17b and 17c): the underprediction of the diffusion is evident and the overall temperature distribution factor (OTDF) is 44.5%, whereas the experimental value is 18.4% (Table 3). In case of constant density calculations, the inclined jets (case 2) gave rise to a more uniform distribution with a pattern factor of 36.2% as opposed to 47.1% for the case of noninclined jets (case 1).

Calculations were also made with a lower turbulent Prandtl number (0.5), but even that was not enough (Fig. 17c and Table 3). The pattern factor, although reduced (35.8%), was still too high by a factor of 2. The overall shape of the distribution is not altered by a reduction of the turbulent Prandtl number (compare Figs. 17b and 17c), and the range of temperatures shown by the calculations (between 560 and 740 K) is still too high compared to the measurements (between 650 and 719 K).

If the following simple empirical formula, from Lefebvre,[1] is used, the overprediction of the mixing parameters is even higher:

$$\mathrm{OTDF} = 1 - \exp\left[-0.05\frac{L}{\Delta D}\left(\frac{U_{\mathrm{jet}}}{U_{\mathrm{ref}}}\right)^2\right]^{-1} \qquad (10)$$

Table 3 Integral parameters of mixing

	OTDF[a]	RTDF[b]	η	Ψ	$T_{\max}$
Experimental	18.4	3.2	93.2	0.06	719
Constant density (case 1)	47.1	9.9	80.3	0.19	765
Variable density (case 3)					
$\sigma_T = 0.9$	44.5	27.9	77.2	0.22	760
$\sigma_T = 0.5$	35.8	19.2	81.6	0.18	740

[a]OTDF = overall temperature distribution factor.
[b]RTDF = radial temperature distribution factor, $= (T_{\max}^{\mathrm{radial}} - T_{\mathrm{mean}})/(T_{\mathrm{mean}} - T_{\mathrm{jet}})$.

where OTDF = $(T_{\max} - T_{\mathrm{mean}})/(T_{\mathrm{mean}} - T_{\mathrm{jet}})$. In this case, an OTDF of 76% is predicted. However, this may not be surprising since the effect of the nozzle has been ignored. This illustrates one of the main limitations of empirical correlations in the design of combustors and shows that the present calculations, although producing results different from the experimental values, can perform better than empirical correlations.

Conclusions

A numerical study of the nonreacting flow inside a dilution system of annular gas turbine combustor was presented. This study assessed the capabilities of a mathematical model for the prediction of the overall parameters of mixing at the outlet section. The following conclusions can be drawn.

1) In case of an insufficient number of grid nodes, the lack of numerical resolution along the circumferential direction caused an underprediction of the streamwise vorticity and could influence the flow in the wake and downstream of the jets. In particular, the lower magnitude of the azimuthal component of velocity associated with the boundary conditions in the longitudinal planes of symmetry may promote the coalescence of the jets and lead to the appearance of spanwise vorticity in their wake.

2) The general flow pattern was predicted adequately and showed that the flow structure at the outlet section was mainly dominated by the outer jet due to the radial location and steeper inclination of the inner wall of the nozzle.

3) The calculations evidenced a lower level of diffusion relative to the measurements. There was a consistent underprediction of the levels of mixing, leading to an OTDF twice as large as the experimental one (even after a reduction of the turbulent Prandtl number from 0.9 to 0.5).

Acknowledgment

This work was supported by a grant from the Ministry of Defence (United Kingdom).

References

[1]Lefebvre, A. H., *Gas Turbine Combustion,* McGraw-Hill, New York, 1983.

[2]Holdeman, J. D., and Walker, R. E., "Mixing of a Row of Jets with a Confined Crossflow," *AIAA Journal,* Vol. 15, No. 2, 1977, pp. 243–249.

[3]Holdeman, J. D., Srinivasan, R., and Berenfeld, A., "Experiments in Dilution Jet Mixing," *AIAA Journal,* Vol. 2, No. 10, 1984, pp. 1436–1443.

[4]Khan, Z. A., McGuirk, J. J., and Whitelaw, J. H., "A Row of Jets in a Crossflow," AGARD-CP308, Paper 10, 1981.

[5]Jones, W. P., and McGuirk, J. J., "Mathematical Modeling of Gas-Turbine Combustion Chambers," AGARD-CP275, Paper 4, 1979.

[6]White, A. J., "The Prediction of the Flow and Heat Transfer in the Vicinity of a Jet in Crossflow," American Society of Mechanical Engineers, Paper 80-WA/HT-26, Nov. 1980.

[7]Claus, R. W., "Analytical Calculation of a Single Jet in Crossflow and Comparison with Experiment," AIAA Paper 83-0238, AIAA 21st Aerospace Sciences Meeting, Jan. 1983.

[8]Andreopoulos, J., "Measurements in a Jet-Pipe Flow Issuing Perpendicularly into a Cross-Stream," *Journal of Fluids Engineering,* Vol. 104, Dec. 1982, pp. 493–499.

[9]Demuren, A. O., "Numerical Calculations of Steady Three-Dimensional Turbulent Jets in Crossflow," *Computer Methods in Ap-*

plied Mechanics and Engineering, Vol. 37, 1983, pp. 309–328.

[10]Green, A. S., and Whitelaw, J. H., "Isothermal Models of Gas-Turbine Combustors," *Journal of Fluid Mechanics,* Vol. 126, 1983, pp. 399–412.

[11]Manners, A. P., "The Calculation of the Flows in Gas Turbine Combustion," Ph.D. Dissertation, Univ. of London, London, England, UK, 1988.

[12]Launder, B. E., "Heat and Mass Transport," *Turbulence,* 2nd ed., Springer-Verlag, Berlin, Germany, 1978, pp. 231–287.

[13]Coupland, J., and Priddin, C. H., "Modelling the Flow and Combustion in a Production Gas Turbine Combustor," *Turbulent Shear Flows V,* Springer-Verlag, Berlin, Germany, 1987, pp. 300–313.

[14]Mongia, H., Reynolds, R., and Srinivasan, R. E., "Multidimensional Gas Turbine Combustion Modeling: Applications and Limitations," *AIAA Journal,* Vol. 4, No. 6, 1986, pp. 890–904.

[15]McGuirk, J. J., private communication, 1984.

[16]Hinze, J. O., *Turbulence,* 2nd ed., McGraw-Hill, New York, 1975.

[17]Jones, W. P., and Launder, B. E., "The Prediction of Laminarisation with a Two-Equation Turbulence Model," *International Journal of Heat and Mass Transfer,* 1972, Vol. 15, pp. 301–314.

[18]Patankar, S. V., *Numerical Heat Transfer and Fluid Flow,* Hemisphere, Washington, DC, 1980.

[19]Shaw, D. F., "An Investigation into the Factors Affecting Randomness in Combustor Exit Temperature Distribution," Rolls-Royce, Rept. PD2181, 1981.

[20]Palma, J. M. L. M., "Mixing in Non-Reacting Gas Turbine Combustor Flows," Ph.D. Dissertation, Univ. of London, London, England, UK, 1989.

[21]Launder, B. E., and Spalding, D. B., "The Numerical Computation of Turbulent Flows," *Computer Methods in Applied Mechanics and Engineering,* Vol. 3, 1974, pp. 269–289.

[22]Crabb, D., and Whitelaw, J. H., "The Influence of Geometric Asymmetry on the Flow Downstream of Row of Jets Discharging Normally into a Free Stream," *Journal of Heat Transfer,* Vol. 101, Feb. 1979, pp. 183–185.